Dipole approximation in the $L_{2,3}$ electron excited spectra in 3*d* transition metals

K. Nuroh*
Department of Mathematical Sciences, Kent State University, Salem, Ohio 44460, USA
(Received 7 July 2008; revised manuscript received 16 October 2008; published 19 December 2008)

A theoretical model based on the autoionization and characteristic decay processes following electron impact ionization of a core electron in solids that has previously been used in calculating electron-energy-loss spectra of transition metals near the $3p$-excitation edge has been extended to the $2p$-excitation edge for ^{21}Sc through ^{27}Ni as well. In the first set of calculations, magnetic effects were ignored and the relative scattering intensity was formulated in terms of the electrostatic interaction $U(p,d)$ between the $3p$ and $3d$ electrons of the intermediate resonant configuration state p^5d^{n+1}, using many-body perturbation theory that led to a generalized Fano-type formula for the intensity profiles. In the second set of calculations in which magnetic effects were included as well, an analysis based on the Bethe-Born formalism of inelastic scattering of electrons on atoms was used. The nature of the relative magnitudes of $U(p,d)$ and the spin-orbit parameters ς_{3p} and ς_{3d} and the localized nature of the $3p$ state necessitated the diagonalization of the intermediate configuration state p^5d^{n+1} to determine the multiplet splitting and their corresponding intensities in the *LS*-coupling limit using fractional parentage scheme. The nonrelativistic multiconfiguration Hartree-Fock (MCHF) code was used in determining the ground and continuum state wave functions, and the itinerant $3d$ states in the solid were approximated with an atomic MCHF-wave function. The outline above is applied to the $2p$-excitation edge, except that because of the relative magnitudes of $U(p,d)$, ς_{2p}, and ς_{3d}, it is found that *LK* coupling is suitable for Sc, Ti, and V, while *jK* coupling is appropriate for Cr to Ni when it comes to the diagonalization of the configuration p^5d^{n+1} to determine the multiplet splitting and their associated scattering intensities. In the dipole approximation, the scattering intensities separate into two distinct manifolds that arise from the $p_{3/2}$ and $p_{1/2}$ states. The branching ratios of the white lines are extracted from the spectra and compared with x-ray-absorption spectra.

DOI: 10.1103/PhysRevB.78.245116 PACS number(s): 71.27.+a, 34.80.Dp, 71.28.+d, 79.20.Ap

I. INTRODUCTION

Because electron-energy-loss spectroscopy (EELS) in reflection mode at intermediate energies (200–2000 eV) probes a veneer of atoms at solid surfaces, it is a useful tool of practical importance in the study of the surface properties of materials. To study the response of electrons using such an external probe from the theoretical standpoint usually requires the knowledge of the surface or the bulk frequency-dependent dielectric function.[1–4] In lieu of the dielectric function, one can also use inelastic scattering of electrons by atoms in the first Born approximation to obtain the scattering cross section.[5–8] In the case of the $3d$-transition metals, at energies that involve the $2p$-core electron, the scattering cross section will be determined essentially by matrix elements involving the $2p \rightarrow 3p$ transitions. In the solid state, the itinerant $3d$-states should in principle be represented by Bloch waves like in the tight-binding approximation. But because the transition matrix elements involve the tightly bound $2p$ orbitals, not much accuracy is lost if the $3d$-Bloch state is approximated by an atomic $3d$ orbital. From this perspective the scattering of the electrons by the metallic surface may be considered as inelastic scattering of electrons by atoms using the Bethe-Born theory. This is the approach taken in this paper.

The question of selection rules in *L*-shell excitations has been addressed extensively in earlier publications. On the one hand, using a model based on analytic representation of both the core and excited electrons, Saldin and Ueda[9] meticulously discussed the validity of the dipole approximation in electron-energy-loss spectroscopy due to *L*-shell excitations of chemical elements with $Z \leq 50$. They found that the dipole approximation is likely to be good for primary energies of the order of 100 keV for all the *L* edges of all the elements studied on the basis of momentum transfer considerations. The use of extended energy loss fine structure (EELFS) technique for studying radial distribution functions for iron and carbidic iron supports the viewpoint that dipole transitions are the most significant contributions in *L*-shell spectra.[10] On the other hand, theoretical calculations based on inelastic scattering of fast electrons by atoms in the limit of the first Born approximation indicate that nondipole transitions become significant in situations where there is a high density of dipole-forbidden states in the near-threshold region.[6] Such cases of optical forbidden transitions have been reported by a number of workers.[11–19] The purpose of this paper is twofold. The first is to discuss the validity of the dipole approximation in resonance *L*-shell excitation spectra specific to the $3d$ transition metals (TMs). The second is to see if there is any trend in resonance peaks as a function of the atomic number *Z* in going from Sc to Ni.

II. FORMULATION WITH ONLY ELECTROSTATIC INTERACTIONS

The main results are contained in Refs. 8 and 20. In particular, Fig. 1 is the set of perturbation diagrams used in arriving at the results in the treatment of the $3p$-excitation edge.[8] It is reproduced here to allow for the identification of interaction matrix elements and their associated self-energy expressions upon which the Fano and other parameters defined in the paper were based. This means transporting the

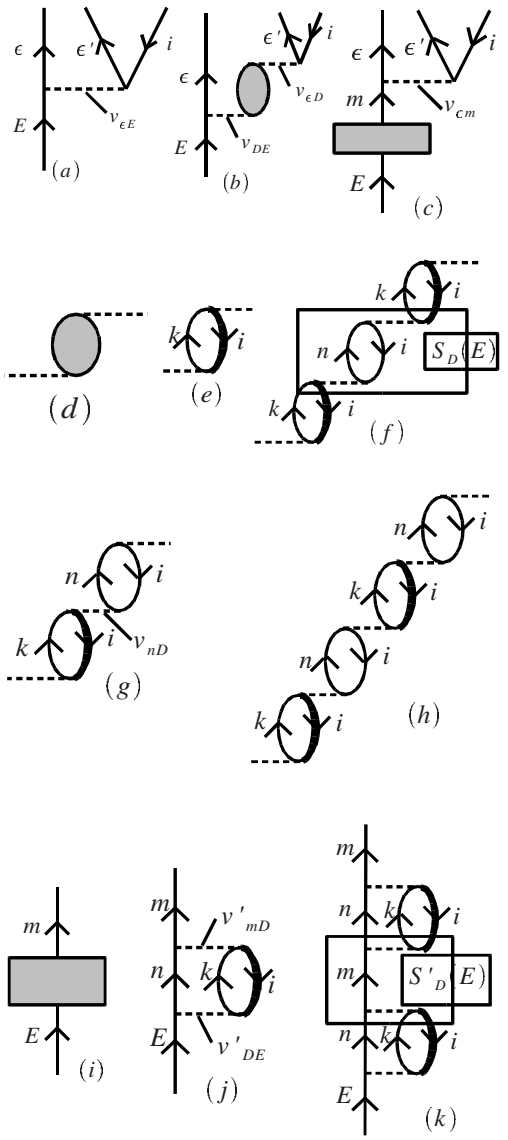

FIG. 1. Amplitude diagrams made up of (a) the basic excitation amplitude; [(b) and (d)–(h)] the resonant contributions from the ring diagrams; and [(c) and (i)–(k)] the resonant contributions from ladder diagrams.

results from the formulation there literatim except wherever the $3p$ orbital appears it is replaced with the $2p$ orbital. As presented there, the main result of the formulation is the total scattering intensity made up of autoionizing and characteristic decay components given by

$$I(E) \sim (v_{\varepsilon E})^2 R(E),$$

$$R(E) = \left[\frac{\gamma(\eta+q)}{\eta^2+1} + \frac{\gamma' q'(\eta+\Delta\eta)}{(\eta+\Delta\eta)^2+1}\right]^2 + \left[\frac{\eta^2+\eta\gamma q-\gamma+1}{\eta^2+1} + \frac{\gamma' q'(\eta+\Delta\eta)-\gamma'}{(\eta+\Delta\eta)^2+1}\right]^2. \quad (1)$$

We reiterate in the above and what follows that any parameter or variable without a prime derives from the ring or bubble diagrams. A parameter with a prime is associated with the ladder diagrams, while a parameter with a double prime is connected with the characteristic decay channel.

In Eq. (1), q and q' are Fano asymmetric line parameters for the respective autoionizing ring and ladder diagrams defined in terms of Coulomb interactions, and are given by

$$q(E) = -\frac{\text{Re } V_{\varepsilon D}(E)}{\text{Im } V_{\varepsilon D}(E)}, \quad V_{\varepsilon D}(E) = v_{\varepsilon D} + \sum \frac{v_{\varepsilon n} v_{nD}}{E_n - E - i\delta}, \quad (2)$$

and

$$q'(E) = -\frac{\text{Re } V'_{\varepsilon D}(E)}{\text{Im } V'_{\varepsilon D}(E)}, \quad V'_{\varepsilon D}(E) = \sum_n \frac{v'_{\varepsilon n} v'_{nD}}{E_n - E - i\delta}, \quad (3)$$

while η and η' are the corresponding Fano reduced energy parameters given by

$$\eta(E) = \frac{\text{Re}[E_D - S_D(E) - S''_D(E)]}{\text{Im}[E_D - S_D(E) - S''_D(E)]}, \quad (4)$$

and

$$\eta'(E) = \frac{\text{Re}[E'_D - S'_D(E) - S''_D(E)]}{\text{Im}[E'_D - S'_D(E) - S''_D(E)]}, \quad (5)$$

with

$$E_n = E_{nf} + E_{\varepsilon d} - E_{3d}, \quad E'_n = E_{nf}, \quad (6)$$

and

$$E_D = E_{\varepsilon d} + E_{3d} - E_{2p}, \quad E'_D = E_{3d} + E_{3d} - E_{2p}. \quad (7)$$

In Eqs. (4) and (5), $S_D(E)$ and $S'_D(E)$ are the interacting self-energies for the autoionizing decay channel for the ring and ladder diagrams, respectively, while $S''_D(E)$ is the self-energy for the characteristic decay channel. These are defined in terms of the bare Coulomb interaction matrix elements as

$$S_D(E) = \sum_n \frac{(v_{Dn})^2}{E_n - E - i\delta}, \quad E_n = E_{nf} + E_{\varepsilon d} - E_{3d}, \quad (8)$$

$$S'_D(E) = \sum_n \frac{(v'_{Dn})^2}{E'_n - E - i\delta}, \quad E'_n = E_{nf}, \quad (9)$$

and

$$S''_D(E) = \sum_n \frac{(v''_n)^2}{E''_n - E - i\delta}, \quad E''_n = E_{nf} - E_{3d} - E_{3d}. \quad (10)$$

Finally, the parameters γ and γ' that appear in Eq. (1) are defined in terms of the bare Coulomb interactions as

$$\gamma = \frac{2\pi(v_{DE})^2}{2\pi[(v_{DE})^2 + (v''_{DE})^2]}, \quad \gamma' = \frac{2\pi(v'_{DE})^2}{2\pi[(v'_{DE})^2 + (v''_E)^2]}, \quad (11)$$

with

TABLE I. Summary of parameters used in calculating the relative intensities as described in the text.

	Sc	Ti	V	Cr	Mn	Fe	Co	Ni
γ'	0.18478	0.18254	0.17464	0.19917	0.18882	0.18785	0.18117	0.18307
γ	0.63519	0.63128	0.59983	0.64676	0.64125	0.65133	0.59999	0.64141
q'	2.2599	2.2000	1.7368	1.5576	1.4473	1.5474	1.5227	1.5471
q	−53.097	−49.248	−32.093	−24.358	−22.989	−26.918	−29.654	−27.737
$\Delta\eta$ (eV)	4367.27	3955.34	2639.21	1560.410	1942.170	2248.53	1766.93	2004.91

$$(v_{DE})^2 = \sum_n (v_{Dn})^2 \delta(E - E_n),$$

$$(v'_{DE})^2 = \sum_n (v'_{Dn})^2 \delta(E - E'_n),$$

$$(v''_E)^2 = \sum_n (v''_n)^2 \delta(E - E''_n). \tag{12}$$

The explicit Coulomb interactions that appear in Eqs. (1)–(3) and in Eqs. (8)–(12) are given in terms of Slater integrals as

$$v_{\varepsilon E} = \sqrt{6}R^1(3d3d;Ef2p) + (2\sqrt{21}/7)R^3(3d3d;Ef2p), \tag{13}$$

$$(v_{Dn})^2 = 4R^1(3d3d;nf2p)^2 + (24/49)R^3(3d3d;nf2p)^2, \tag{14}$$

$$\begin{aligned}(v'_{Dn})^2 = {} & (14/15)R^1(3d3d;nf2p)^2 \\ & - (24/175)R^1(3d3d;nf2p)R^3(3d3d;nf2p) \\ & + (96/1225)R^3(3d3d;nf2p)^2,\end{aligned} \tag{15}$$

and

$$\begin{aligned}(v''_n)^2 = {} & (34/15)R^1(3d3d;nf2p)^2 \\ & - (8/35)R^1(3d3d;nf2p)R^3(3d3d;nf2p) \\ & + (16/35)R^3(3d3d;nf2p)^2.\end{aligned} \tag{16}$$

Note that $E_{\varepsilon d} \equiv E_{3d}$, and this makes $E_n = E'_n$. We also note that in Eq. (1), $(\eta + \Delta\eta)$ replaces $(\eta - \Delta\eta)$ in the original analysis.[20] This is because $\Delta\eta = \eta - \eta'$ was so defined to make $\Delta\eta > 0$ for La and Ce. For the TMs, we have to interchange the roles of η and η', and instead set

$$\begin{aligned}\Delta\eta = \eta' - \eta = {} & \frac{\mathrm{Re}[E'_D - S'_D(E) - S''_D(E) - E]}{\pi[(v'_{DE})^2 + (v''_E)^2]} \\ & - \frac{\mathrm{Re}[E_D - S_D(E) - S''_D(E) - E]}{\pi[(v_{DE})^2 + (v''_E)^2]}.\end{aligned} \tag{17}$$

In consonance with the approximations used in Sec. III for the computation of the multiplet energies in which the intraelectrostatic interactions of the $3d^n$ electrons of the intermediate $2p^5 3d^{n+1}$ are neglected, we set $\gamma' = 0$ in Eq. (1) to exclude characteristic contributions yielding the autoionizing scattering intensity

$$R_A(E) = \left[\frac{(\eta + \gamma q)^2 + (\gamma - 1)^2}{\eta^2 + 1}\right]. \tag{18}$$

The computational description of the parameters that appear in Eqs. (2)–(17) is pretty much the same as has been described in the $3p$-excitation case[8] if the $3p$ orbital is swapped for the present $2p$ situation in the MCHF and CMCHF codes. Also all the quadratic interaction functions used in the computation of the principal value integrals fit excellently to a logarithmic-normal function and have accordingly been obtained using MATHEMATICA's adaptive quadrature that produces the same numerical results as the quadrature described in the $3p$-excitation case.[8] The evaluated parameters are found in Table I, and the results of the calculation for the expression $R(E)$ are shown in Fig. 2.

III. FORMULATION INCLUDING MAGNETIC INTERACTIONS

A. Energy matrices

The reaction equation of the scattering process is

$$E + p^6 d^n \rightarrow \varepsilon + p^5 d^{n+1}. \tag{19}$$

The diagonalization of the $p^5 d^{n+1}$ resonant intermediate configuration should be treated differently for the $2p$ and $3p$ electrons. In the $3p$ case, because the $3p$ and $3d$ orbitals overlap significantly, the $3p$ hole is expected to interact strongly with the d^n electrons of the ground state, and it was necessary to consider an antisymmetrized wave function in which the d^{n+1} electrons were treated on equal footing through the use of the fractional parentage scheme. In the present $2p$ case, however, since the $2p$ hole is more localized than the d orbital, the d^n electrons of the ground configuration may be neglected, and the interaction between the $2p$ hole and the excited optical d electron is expected to dominate the spectrum. This means that the diagonalization of the $p^5 d^{n+1}$ configuration essentially is that of the $2p3d$ electron-hole, namely, a two-particle configuration $nlsn'l's'$, where $nls(1) \rightarrow 2p$, and $n'l's'(2) \rightarrow 3d$. The next question is the type of coupling to employ. Following Cowan,[21] for the situation in which

$$(r_{12}^{-1})_{\mathrm{dir}} > h_{so}(1), \quad h_{so}(2), \quad h_{so}(1) > (r_{12}^{-1})_{\mathrm{exch}}, \tag{20}$$

the quantum numbers specified by $L[K]_J$ of the coupled state $|[(ll')L,s]K,s',J\rangle$ are good quantum numbers. On the other hand, in situations whereby

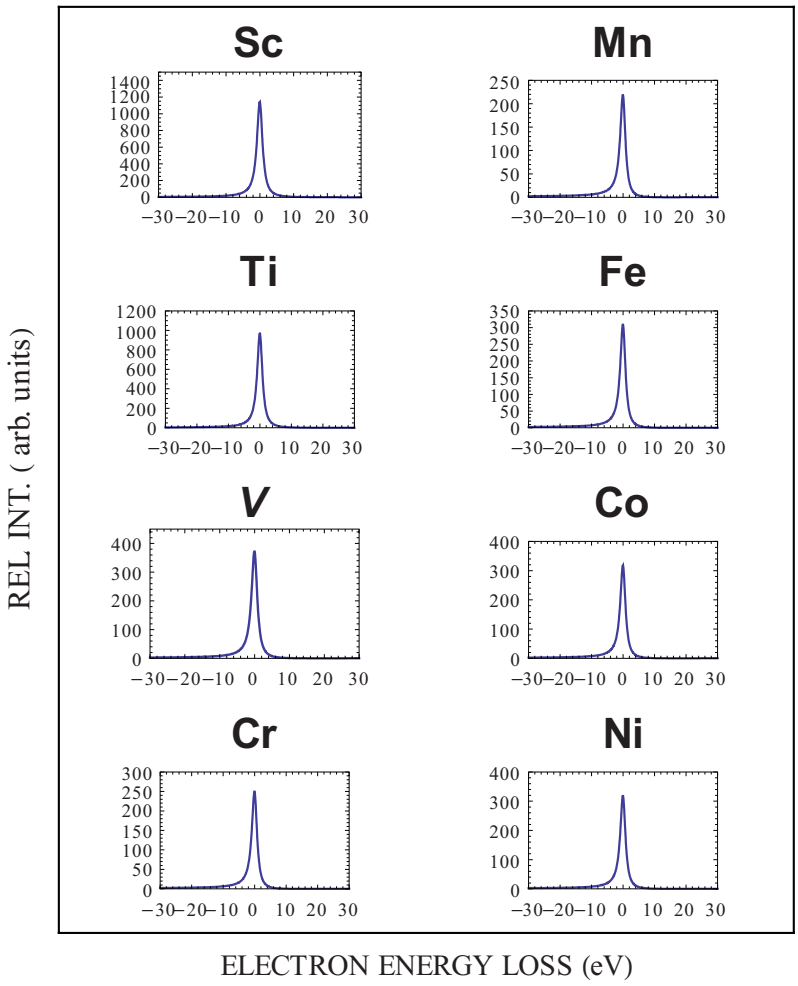

FIG. 2. (Color online) The relative intensities (arbitrary units) for the TMs.

$$h_{so}(1) \geq (r_{12}^{-1})_{\mathrm{dir}} > (r_{12}^{-1})_{\mathrm{exch}} > h_{so}(2), \tag{21}$$

the quantum numbers specified by $(jK)_J$ of the coupled state $|[(ls)_j, l']K, s', J\rangle$ are good quantum numbers. The multiplet energies of the $nln'l'$ configuration in LK coupling are given by

$$\Delta E(L[K]_J) = \{\Delta E_{\mathrm{dir}}(L[K]_J) - \Delta E_{\mathrm{exch}}(L[K]_J) + \Delta E_{so}^{nl}(L[K]_J) + \Delta E_{so}^{n'l'}(L[K]_J)\}. \tag{22}$$

The corresponding multiplet energies of the $nln'l'$ configuration in jK coupling are given by

$$\Delta E[(jK)_J] = \{\Delta E_{\mathrm{dir}}[(jK)_J] - \Delta E_{\mathrm{exch}}[(jK)_J] + \Delta E_{so}^{nl}[(jK)_J] + \Delta E_{so}^{n'l'}[(jK)_J]\}. \tag{23}$$

The explicit expressions for ΔE_{dir}, ΔE_{exch}, ΔE_{so}^{nl}, and $\Delta_{so}^{n'l'}$ in LK- and jK-couplings are left to the Appendix. The spin-orbit and Slater radial integrals used in the diagonalization of the energy matrices are found in Table II. We see from these values that the condition stated in Eq. (20) applies to Sc, Ti, and V, while the condition stated in Eq. (21) applies to Cr to Ni. Accordingly, the LK-coupling scheme is used for Sc, Ti,

TABLE II. The $2p$ and $3d$ spin-orbit parameters, and Slater radial integrals used in the diagonalization of the multiplet energy matrices. Γ is the total autoionizing broadening width comprising ring and ladder diagram contributions from Sec. II using Eq. (30). All energies are in electron volts (eV).

	Sc	Ti	V	Cr	Mn	Fe	Co	Ni
ς_{2p}	2.83	3.53	4.35	5.31	6.41	7.68	9.13	10.77
ς_{3d}	0.01	0.02	0.02	0.03	0.04	0.05	0.07	0.08
$F^2(2p,3d)$	3.13	3.85	4.45	4.36	5.56	6.01	6.48	6.96
$G^1(2p,3d)$	1.97	2.68	3.01	2.96	3.92	4.30	4.70	5.10
$G^3(2p,3d)$	1.12	1.43	1.70	1.68	2.22	2.44	2.67	2.90
Γ	0.21	0.29	0.42	0.66	0.89	0.83	0.82	0.96

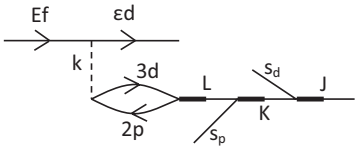

FIG. 3. The angular-momentum graph in *LK* coupling for calculating the excitation amplitude for Sc, Ti, and V.

and V, while the *jK*-coupling scheme is used for Cr to Ni in the calculation of the multiplet energies and transition amplitudes.

B. Excitation amplitudes

Figure 3 is the amplitude diagram in *LK* coupling for Sc, Ti, and V that evaluates to the expression

$$a(L,K,J) = [K,J/L]^{1/2} \times [d,f,d,p]^{1/2} \sum_k R^k(Ef2p;\varepsilon d3d) \times \begin{pmatrix} d & k & f \\ 0 & 0 & 0 \end{pmatrix} \begin{pmatrix} d & k & p \\ 0 & 0 & 0 \end{pmatrix} \delta(k,L), \tag{24}$$

where $[a,b/c,\ldots]=(2a+1)(2b+1)/(2c+1)\cdots$ in the above and what follows.

Figure 4 is the amplitude diagram in *jK* coupling for Cr to Ni. The diagram evaluates to the expression

$$b(j,K,J) = [j,K,J]^{1/2} \times [d,f,d,p]^{1/2} \sum_k R^k(Ef2p;\varepsilon d3d) \times \begin{pmatrix} d & k & f \\ 0 & 0 & 0 \end{pmatrix} \begin{pmatrix} d & k & p \\ 0 & 0 & 0 \end{pmatrix} \begin{Bmatrix} k & s_p & K \\ j & d & p \end{Bmatrix}. \tag{25}$$

Following the Bethe-Born analysis of the inelastic electron scattering on atoms presented in Ref. 5 and recapitulated in Ref. 8, the relative scattering cross section for $2p \rightarrow 3d$ transitions is essentially determined by the correlation part of the atomic form factor given by

$$F^{\text{corr}}_{\text{Born}}(Q,\varepsilon) = 1 - W(Q,\varepsilon) \sum_\mu \frac{A_\mu(\varepsilon,E)}{E_\mu - \varepsilon - i\delta}, \tag{26}$$

where $A_\mu \rightarrow a(L,K,J)$ for Sc, Ti, and V, and $A_\mu \rightarrow b(j,K,J)$ for Cr to Ni, and the radial weighted integrated spherical Bessel function $W(Q,\varepsilon)$ is given by

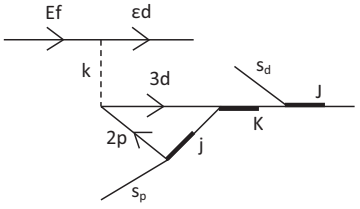

FIG. 4. The angular-momentum graph in *jK* coupling for calculating the excitation amplitude for Cr to Ni.

$$W(Q,\varepsilon) = \sum_\nu \int dr P_{3d}(r) j_\nu(Qr) \times P_{2p}(r) / \sum_\nu \int dr P_{\varepsilon d}(r) j_\nu(Qr) P_{2p}(r). \tag{27}$$

In the above, $j_\nu(Qr)$ is the spherical Bessel function of integral order ν, and Q is the momentum transfer of the impinging electron to the atom. In the numerical calculations presented here, we have taken εd to be $3d$ making $W(Q,\varepsilon)=1$, and hence, rendering the correlation part of the of the atomic form factor to become independent of the momentum transfer Q. Under these conditions, the scattering cross section may be represented by the dimensionless relative intensity

$$R_B(\eta) = |F^{\text{corr}}_{\text{Born}}(Q,\varepsilon\ |^2 = \left| 1 + \sum_\mu \frac{A_\mu(E)}{\eta - \Delta E_\mu + i\Gamma_\mu} \right|^2. \tag{28}$$

In Eq. (28) above, η is the electron-energy-loss parameter in the sense as used in Sec. II relative to the $2p \rightarrow 3d$ excitation and defined by

$$\eta = E - E_{3d} - E_{3d} + E_{2p} - \text{Re}[S_d(E)], \tag{29}$$

while ΔE_μ are the multiplet energies given in Eqs. (22) and (23) and Γ_μ is the total autoionizing broadening width given by

$$\Gamma_\mu(E) = 2\pi[(v'_{DE})^2 + (v_{DE})^2]. \tag{30}$$

The multiplet intensities are shown in Fig. 5. Both $A_\mu(E)$ and $\Gamma_\mu(E)$ are evaluated at the peak values of $R^{1,3}(Ef2p;3d3d)$ while $\Gamma_\mu(E)$ is evaluated at the $3d \rightarrow 2p$ excitation energy with the results in Table II. Figure 6 shows representative distribution of these radial integrals for Sc, Cr, and Ni. We observe that the peak values increase in magnitude and the distribution broadens gradually in going from Sc to Ni.

In the radial integral $R^k(Ef2p;3d3d)$, on the basis that $R^3 < R^1$ we may neglect the $k=3$ contributions and retain only the $k=1$ contributions. This would lead to only $J=1$ contributions in the excitation amplitudes in both the *LKJ* and *jKJ* couplings. The net effect due to the triangular conditions on the angular momenta is that the $L[K]_J$-multiplet levels become the two-level labels $1[\frac{1}{2}]_1$ and $1[\frac{3}{2}]_1$, while the $(jK)_J$-multiplet levels become the three-level labels $(\frac{1}{2}\frac{3}{2})_1$, $(\frac{3}{2}\frac{1}{2})_1$, and $(\frac{3}{2}\frac{3}{2})_1$. However, the $(\frac{1}{2}\frac{3}{2})_1$ and $(\frac{3}{2}\frac{1}{2})_1$ states have the same transition matrix element, and because the energy level of the multiplet $(\frac{3}{2}\frac{1}{2})_1$ is juxtaposed to that of $(\frac{3}{2}\frac{3}{2})_1$ these two blend together to essentially give a two-level structure that may be characterized as $(\frac{1}{2}\frac{3}{2})_1$ and $(\frac{3}{2},\frac{1}{2}\frac{3}{2})_1$ originating from $p_{1/2}$ and $p_{3/2}$ spin-orbit splitting of the $2p$ state. As a consequence, the pair of levels $1[\frac{1}{2}]_1$, $1[\frac{3}{2}]_1$ in *LKJ* coupling for Sc, Ti, and V, and the pair of levels $(\frac{1}{2}\frac{3}{2})_1$, $(\frac{3}{2},\frac{1}{2}\frac{3}{2})_1$ in *jKJ* coupling for Cr to Ni are to be identified with the observed $L_{2,3}$ levels in the transition metals Sc through Ni. These two pairs of multiplets and their corresponding transition amplitudes are calculated and the results are shown in Fig. 7.

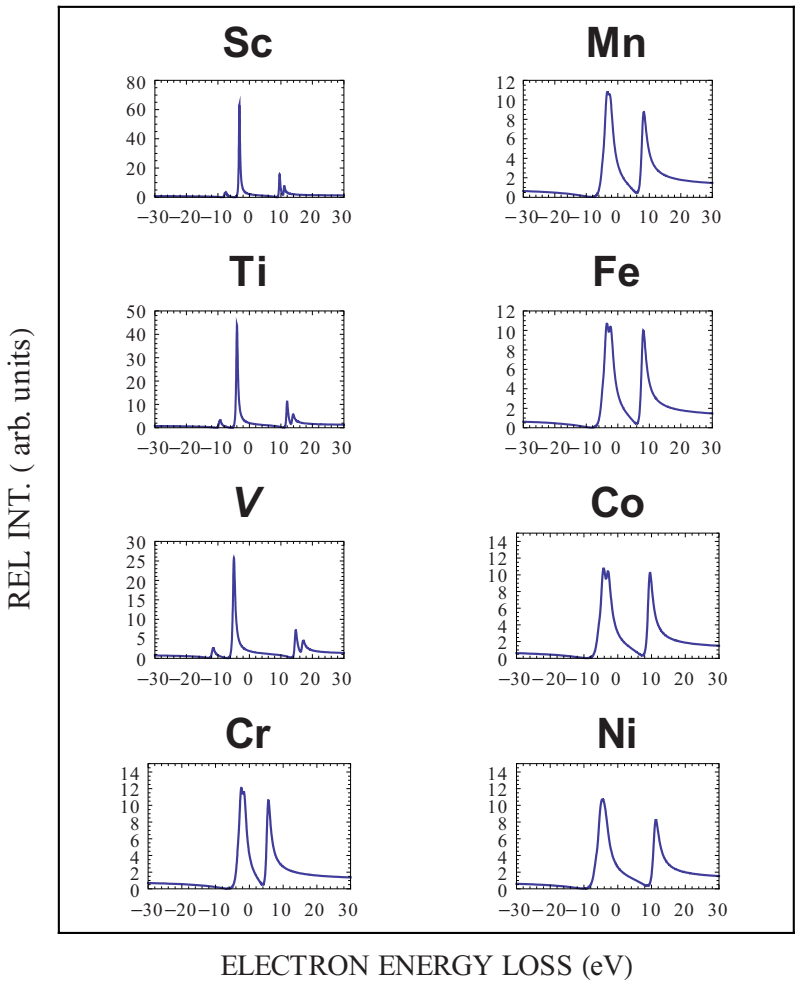

FIG. 5. (Color online) The multiplet electron-energy-loss intensities (in arbitrary units) for Sc through Ni.

IV. RESULTS AND DISCUSSION

Without spin-orbit interactions the multiplets in *LKJ* coupling are degenerate in K and J resulting in the two levels provided by $L=1,3$. When the spin orbit of the $2p$ hole is included, the degeneracy with respect to K is lifted resulting in four multiplets provided by $K=1/2$, 3/2, 5/2, and 7/2. As we can see from Table II, the spin-orbit parameter of the $3d$ electron can be neglected without affecting the positions of the *LK* multiplets appreciably. However, its inclusion is necessary to lift the degeneracy with respect to J leading to a total of eight multiplets comprising of one $J=0$, two $J=1$, two $J=2$, two $J=3$, and one $J=4$. Similar analysis for the *jKJ* coupling leads to a total of 12 multiplets. In either case, the level structure is made up of two clusters originating from $K=1/2,5/2$ and $K=3/2,7/2$ in *LK* coupling, and $j=1/2$ and $j=3/2$ in *jK* coupling.

First, we provide some details in the calculated spectra. The spectra shown in Fig. 2 were obtained using the expression $R(E)$ from Eq. (1). The autoionizing intensity expression $R_A(E)$ produced intensity distributions not markedly different from those shown in Fig. 2. This indicates that characteristic decay events are insignificant in the $2p$-edge EELS. The masking or suppression of these characteristic events is traceable to the huge numbers for $\Delta\eta$ in the $2p \rightarrow 3d$ excitations. For this reason, the spectra in Fig. 2 may be characterized as autoionizing with only electrostatic interactions included. What the calculation conveys is that if the various TMs were prepared under the same experimental

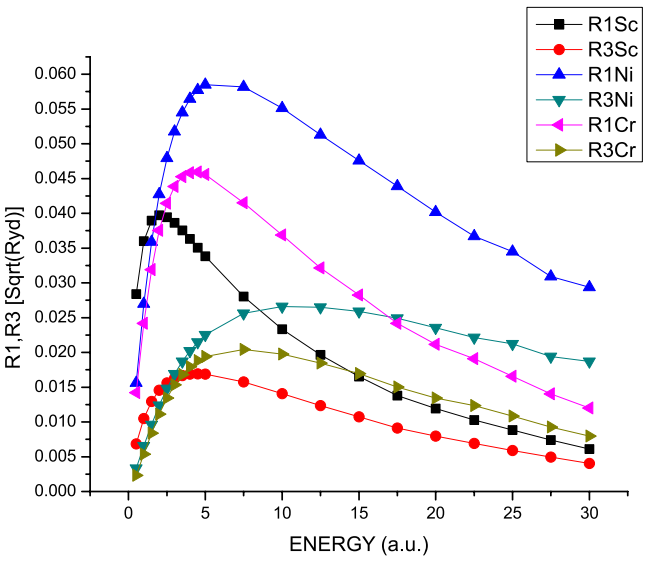

FIG. 6. (Color online) The continuum Slater radial integrals for Sc, Cr, and Ni with $R1$, $R3=R^{1,3}(Ef2p;3d3d)$ (1 hartree=2 Ry =1 a.u.).

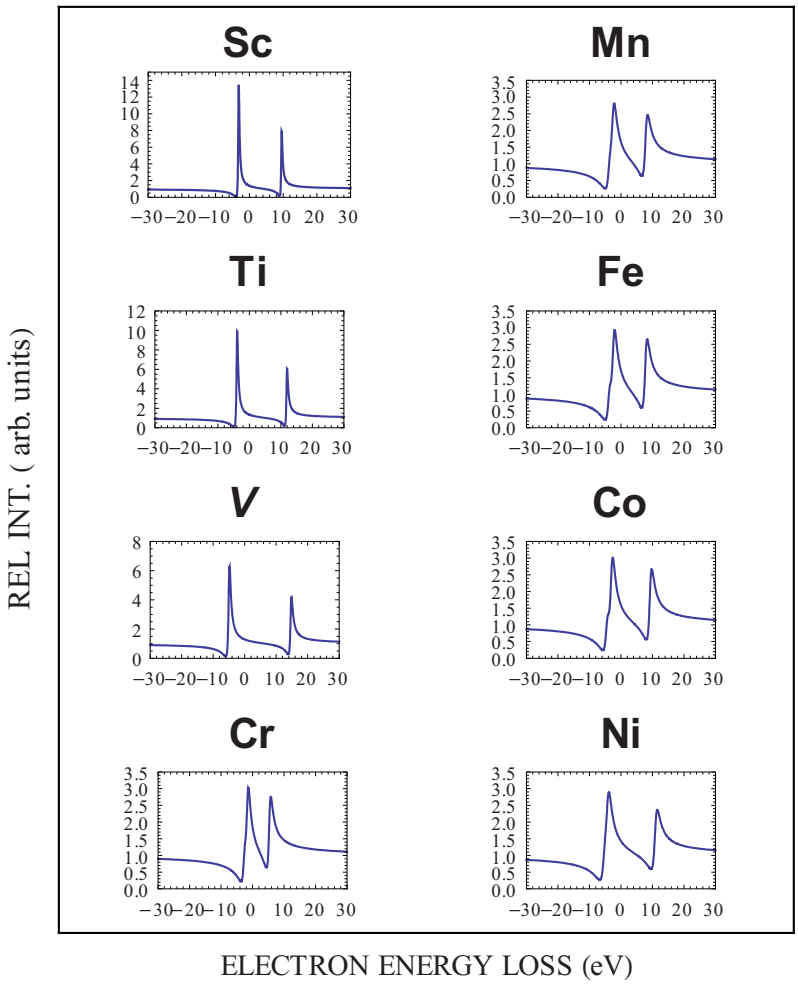

FIG. 7. (Color online) The multiplet electron-energy-loss intensities (in arbitrary units) in the dipole approximation for Sc to Ni.

conditions, the measured resonance peak in Sc would be the largest followed by Ti and V in that order: the rest of the TMs would have roughly the same resonance peaks. This trend should persist even if magnetic effects are included, relative wise. This is evident if the L_3 resonance is examined in either Figs. 5 and 7. Figure 5 shows the relative intensities for the TMs when all the multiplet levels are included. For Cr to Ni, we have two distinct broadened structures that may be characterized with the L_3 and L_2 edges. For Sc, Ti, and V on the other hand, not only are the L_3 and L_2 resonances narrower but each one has some associated shoulders with the L_2 resonance less intense compared with the L_3 resonance. If, however, the dipole approximation is invoked, we then have the picture of the spectra for the various TMs in Fig. 7. In Fig. 7, we observe that the L_3 resonance peak is larger than the L_2 peak and the ratio L_3/L_2 of the resonance peaks is of the order of 1.41 for all the TMs. Here we see the same trend in the resonance peaks of the L_3 structure just as those in Fig. 2. To make it easier for possible future experimental comparison with the theoretical data, we have reported the $2p \rightarrow 3d$ relative resonance peak values from Fig. 2 and the corresponding L_3 resonance peaks from Fig. 7 in Table III.

$L_{2,3}$ EELS measurements have been reported by Leapman *et al.*[14] for metallic Ti, Cr, Fe, and Ni. Similar measurements have been reported by Lozzi *et al.*[22] for Cr, and Hitchcock and Teng[23] for Ni. The data in Refs. 14 and 22 for Cr and Refs. 14 and 23 for Ni agree. The theoretical data for the spectra using the dipole approximation in Fig. 7 are in good agreement with the measurements for Cr, Fe, and Ni. In the case of Ti, the measurement of Ref. 14 indicates that the L_3 resonance peak is smaller than the L_2 peak. This picture is confirmed by photoabsorption measurements by Ref. 24. However, the theoretical calculation predicts the opposite:

TABLE III. The resonance peak values extracted from Figs. 2 and 7 for the L_3 structure. These are labeled respectively as ResPeak1 and ResPeak3.

	Sc	Ti	V	Cr	Mn	Fe	Co	Ni
ResPeak1	1137.6	966.6	370.7	248.3	217.4	316.7	316.7	316.7
ResPeak3	13.47	9.89	6.30	3.03	2.80	2.93	3.01	2.85

the one presented here for Ti is in accord with theoretical density-functional theory (DFT)–based photoabsorption spectra calculation using linearized augmented plane wave (APW) method that predicts the L_3 resonance peak larger than the L_2 peak.[25] Since the APW method exploits the itinerant character of the $3d$ state, the discrepancy between the theoretical calculations and measurement cannot be attributed to lack of using a Bloch wave function in the case of the present atomic-based calculations. Perhaps some of the suggestions made in Sec. V might be the answer in rectifying the theoretical calculations to match the experimental data.

Soft x-ray appearance potential spectroscopy (SXAPS) is a technique in which surfaces of solids are bombarded with electrons of energy E. If the primary electron energy E is adequate to excite a core electron, then in the de-excitation process photons are emitted. The emitted photon intensity is measured as a function of E. Apart from the fact that the dipole matrix element between the core and optical electrons (here, $\langle 2p|r\cos\theta|3d\rangle$) enter the expression for the excitation amplitude,[26] and because the dipole selection rule is valid in SXAPS, this makes the dipole approximation results presented here suitable for comparison with L-shell SXAPS in the TMs. In fact the results in Fig. 7 for Sc to Ni compare very well with the SXAPS measurements by Park and Houston.[27] In light of the good qualitative agreement between the dipole approximation results in Fig. 7 and the available measurements, we are led to conclude that L-shell electron excited spectra obey the dipole selection rules, thus validating the conclusions arrived at by Saldin and Ueda.[9]

Once a core electron is excited in either EELS or in XAS, the line broadening of the created core hole emanates mainly from two decay processes, namely, autoionization and characteristic or Auger. In XAS the absorption line strengths are due to the dipole operator and in EELS, the scattering line strengths are due to Coulomb interactions. It is, therefore, expected that the absorption spectral widths in XAS would be similar to the scattering cross section widths in EELS. From this perspective, the calculated $L_{2,3}$ spectra in the present work may be compared with XAS data in the literature. In fact, de Groot[28] gave a comprehensive review of XAS and dichroism of the transition metals and their compounds, replete with experimental data and various theoretical approaches, and the reader is referred to the article and the references therein for details. In particular, the works of Thole and van der Laan[29] and Waddington *et al.*[30] are selected for discussion because (1) they contain data for the branching ratios of all the systems considered in this paper, and (2) their theoretical approaches have some fundamental tenets with the approach in this paper. In this paper, an atomic multiplet theory is used to describe the $L_{2,3}$ spectra in the solid. Perhaps the weakest point of the paper is that the $3d$ state in the solid is represented by a quasiatomic state via a $3d$-MCHF wave function. However, since the mere nature of the MCHF code includes some correlations of the $4s$ state, some itinerant electronic features of the solid such as the electron s and p states are included but certainly not as ideal as a Bloch-type representation of the $3d$ state.

Thole and van der Laan[29] also used an atomic multiplet theory, but incorporates the solid state environment via a ligand field theory that had been proposed earlier.[31–34] Based on this general approach, they formulated rules that allowed for the direct calculation of the branching ratio of the white lines in the transition metals and their compounds without resorting to complicated crystal-field calculations. The general trend in their calculation is a separation of the branching ratio into two parts in the $3d$ transition metals: the high-spin and low-spin values (in the crystal-field terminology) at the high end of the d^n occupancy ($n=4-8$) with the high-spin values larger than the low-spin values. Both values then decrease gradually to converge to the same values for the low end of the d^n occupancy ($n=1-3$). An observation made in their analysis is that for the $3d$ transition metals, the crystal-field effects may be neglected with little effect on the determination of the branching ratio.

Branching ratio calculations in XAS for $L_{2,3}$ white line have been reported by Waddington *et al.*[30] using the atomic multiconfiguration Dirac-Fock (MCDF) code of Grant *et al.*[35] to calculate atomic wave functions, and a modified version of the transition-rate code used by Dyall and Grant[36] to determine the line strengths. The calculation of the multiplets was carried in the jj-coupling limit, and they used a $3d$-MCDF wave function for the itinerant $3d$ state justifying its usage on the basis that the d wave function is relatively localized and the d band being narrow. The results of their $L_3:L_2$ peak ratios for the $3d$ transition metal atoms and ions have been compared with different measurements and theoretical calculations. For this reason, no comparison with those data will be made here. Instead, the results from the present calculation will be compared with those of Waddington *et al.*[30] From their $L_3:L_2$ peak ratios, I have calculated the peak-height branching ratio defined as $H_3/(H_2+H_3)$ indicated by the WLTR legend in Fig. 8. The data for Sc, Ti, V, Cr^{3+}, Mn^{2+}, Fe^{2+}, Co^{2+}, and Ni^{2+} from Ref. 30 were used. The corresponding peak-height branching ratio extracted from Fig. 7 is shown in Fig. 8 as the peak-height branching ratio (BRH) legend. Also shown in Fig. 8 as the integrated area branching ratio (BRA) legend is the integrated area branching ratio defined as $I(L_3)/[I(L_2)+I(L_3)]$. The arrow on the right side of Fig. 8 indicates the statistical value 2/3 for the $p_{3/2}$, $p_{1/2}$ states. As was pointed out in Ref. 30, measuring the change in the ratio of the areas can give different results in those areas where the spectra have different manifolds. In determining $I(L_3)$ and $I(L_2)$, the continuum background of the spectra was first subtracted and each manifold fitted with a Gaussian such that the full width at half maximum (FWHM) of the manifold and the Gaussian distribution were the same. With the exception of Sc, we find that both the peak height and the integrated branching ratios are below the statistical value, and the values are not that much different from one another. In the case of the calculated values using the data from Ref. 30, Sc and Ti are below the statistical value while V and Cr^{3+} are almost at the statistical value, but Mn^{2+}, Fe^{2+}, Co^{2+}, and Ni^{2+} are above the statistical value. Since the integrated branching ratio for Sc, Ti, and V are about the same as the peak-height branching ratio of Ref. 30, one is led to suspect that that the larger values for Cr^{3+}, Mn^{2+}, Fe^{2+}, Co^{2+}, and Ni^{2+} originate from the ionization.

There should somehow be a connection between the formulation in Sec. II without magnetic interactions and Sec. III

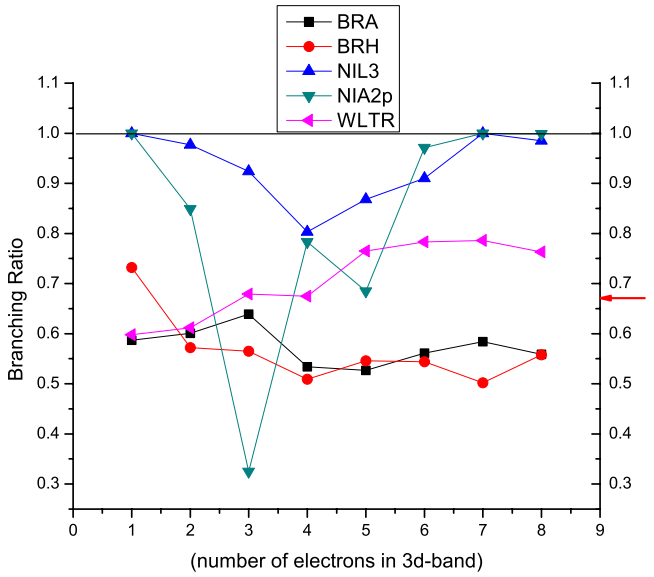

FIG. 8. (Color online) The branching ratio (BR) of the 3*d* transition metals as described in the text. BRA legend (integrated BR from the present work); BRH legend (peak-height BR from the present work); NIL3 legend (integrated normalized and relative L_3-edge area); NIA2*p* legend (integrated normalized and relative 2*p*-edge area); WLTR-legend (peak-height BR calculated with data from Ref. 30).

with magnetic interactions. A possible way to establish this connection is through the integrated areas $I(2p)$ for the 2*p*-edge spectra in Fig. 2 and $I(L_3)$ in Fig. 7. Since the line strengths are based on two different coupling limits, it is natural to separate the analysis into two groups comprising the low-end 3*d*-occupancy systems (Sc, Ti, and V) and the high-end 3*d*-occupancy systems (Cr, Mn, Fe, Co, and Ni). In each group, the system with the largest integrated area is normalized to unity, and the other areas are determined relative to these. In the low-end group it is Sc, and in the high-end group it is Co. The results of the calculation are represented by the NIA2*p*-legend for the 2*p*-edge spectra, and the NIL3-legend for the L_3-edge spectra. Apart from V on the low-end systems, and Mn on the high-end systems, the general trend is one of a gradual decrease for the low-end group, about the same at Cr, and a gradual increase for the high-end group.

V. CONCLUSIONS

The 2*p*-edge excitation spectra in the 3*d* transition metals have been treated using many-body perturbation theory that led to a generalization of the Fano asymmetric line shape expression. Under certain limiting conditions,[20] this generalized Fano expression in Eq. (1) reduces to the familiar Fano asymmetric formula $I(\eta)=(\eta+q)^2/(\eta^2+1)$ or $I(\eta)=(\eta+q')/(\eta^2+1)$ for the retention of only the ring or ladder diagrams, respectively, in the perturbation. Magnetic effects were excluded in the treatment. With the inclusion of magnetic effects, the Bethe-Born theory was invoked, and the line strengths for Sc, Ti, and V were calculated in the *LK* coupling limit, while the line strengths for Cr, Mn, Fe, Co, and Ni were calculated in the *jK* coupling limit. With the retention of only dipole contribution to the Coulomb excitation amplitude, the calculated spectra separate into two manifolds that are traceable to the $2p_{3/2}(L_3)$ and $2p_{1/2}(L_2)$ edges. The calculated branching ratio of the white lines shows an almost uniform systematic trend but whose values are below the statistical value of 2/3, and compares well with calculations based on *jj* coupling. The calculations demonstrate that *LK* and *jK* couplings provide alternative routes to intermediate and *jj* couplings, and other theoretical models for the discussion of core-level excitation spectra in the intermediate energy region.

The calculations, however, can be improved upon if the following additional considerations are factored in:

(1) Magnetic effects should be included in the perturbation approach in Sec. II to make it possible to directly compare with $L_{2,3}$ measurements and other theoretical models.

(2) To realistically describe the solid state, the 3*d* state will have to be represented by a Bloch-type wave function or one that takes into account the band structure of the *s* and *d* states.

(3) Only the optical *d* electron was included in the p^5d^{n+1} configuration to determine the multiplet splitting. The consequence of this is that only autoionization decay broadening is included in the calculations. To include characteristic decay broadening, the other d^n electrons will have to be considered as well. This would certainly affect the spectral linewidths and in turn the branching ratio.

(4) Two-hole scattering events are absent in the present treatment. Inclusion of such events might be necessary to address satellite and shakeup effects that have been reported in EELS measurements,[14] and which are necessary in energy-loss near-edge structure (ELNES) studies.[37,38]

The analysis presented here can be instructive for future studies in the *M*-shell spectra of the rare-earth metals, and in particular, to investigate the breakdown of the dipole approximation that has been reported in the light lanthanides.[16,17]

APPENDIX: ELECTROSTATIC AND SPIN-ORBIT INTERACTION MATRIX ELEMENTS IN *LK* AND *jK* COUPLINGS

The angular-momentum graphical techniques described in the book by Lindgren and Morrison[39] are used in determining the diagonal energy matrices in which the *LK*- and *jK*-coupled configuration states, the two-body direct and exchange Coulomb interactions, and the single-body spin-orbit interactions are set up, coupled, and evaluated using the theorems of Jucys *et al.*[40] The final expressions in *LK* coupling are

$$\Delta E_{\rm dir}[L(K)_J] = \langle [(ll')L,s]K,s',J|(r_{12}^{-1})_{\rm dir}|[(ll')L,s]K,s',J\rangle$$
$$= \sum_k (-1)^l [l,l'] \begin{pmatrix} l & k & l \\ 0 & 0 & 0 \end{pmatrix} \begin{pmatrix} l' & k & l' \\ 0 & 0 & 0 \end{pmatrix} \times \begin{Bmatrix} l & l & k \\ l' & l' & L \end{Bmatrix} F^k(nl,n'l'), \quad \text{(A1)}$$

$$\Delta E_{\mathrm{exch}}[L(K)_J] = \langle [(ll')L,s]K,s',J|(r_{12}^{-1})_{\mathrm{exch}}|[(ll')L,s]K,s',J\rangle = (-1)^L \sum_k [l,l'] \times \begin{pmatrix} l & k & l' \\ 0 & 0 & 0 \end{pmatrix}^2 \begin{Bmatrix} l & l' & L \\ l & l' & k \end{Bmatrix} G^k(nl,n'l'), \quad \text{(A2)}$$

$$\Delta E_{so}^{nl}[L(K)_J] = \langle [(ll)L,s]K,s',J|h_{so}(nls)|\ (ll)L,s]K,s',J\rangle = (-1)^{K+s+l+l'+1}[L] \begin{Bmatrix} L & L & 1 \\ s & s & K \end{Bmatrix} \times \varsigma_{nl}[(3/2)l(l+1)(2l+1\ ]^{1/2}, \quad \text{(A3)}$$

$$\Delta E_{so}^{n'l'}[L(K)_J] = \langle [(ll')L,s]K,s',J|h_{so}(n'l's') \times |[(ll')L,s]K,s',J\rangle = (-1)^{J+l+l'+1}[L,K] \times \begin{Bmatrix} K & K & 1 \\ L & L & s \end{Bmatrix} \begin{Bmatrix} L & L & 1 \\ l' & l' & l \end{Bmatrix} \varsigma_{n'l'}[(3/2)l'(l'+1)(2l'+1)]^{1/2}. \quad \text{(A4)}$$

The corresponding results in jK coupling are

$$\Delta E_{\mathrm{dir}}[(jK)_J] = \langle [(ls)j,l']K,s',J|(r_{12}^{-1})_{\mathrm{dir}}|[(ls)j,l']K,s',J\rangle = [j](-1)^{K+s+2j} \sum_k [l,l'] \begin{pmatrix} l & k & l \\ 0 & 0 & 0 \end{pmatrix} \begin{pmatrix} l' & k & l' \\ 0 & 0 & 0 \end{pmatrix} \times \begin{Bmatrix} j & j & k \\ l & l & s \end{Bmatrix} \begin{Bmatrix} j & j & k \\ l' & l' & K \end{Bmatrix} F^k(nl,n'l'), \quad \text{(A5)}$$

$$\Delta E_{\mathrm{exch}}[(jK)_J] = \langle [(ls)j,l']K,s',J|(r_{12}^{-1})_{\mathrm{exch}}|[(ls)j,l']K,s',J\rangle = [j](-1)^{K+s} \sum_k [l,l'] \begin{pmatrix} l & k & l' \\ 0 & 0 & 0 \end{pmatrix}^2 F^k(nl,n'l') \times \sum_{l''} (-1)^{l''}[l''] \begin{Bmatrix} l & l' & l'' \\ l & l' & k \end{Bmatrix} \begin{Bmatrix} K & s & l'' \\ l & l' & j \end{Bmatrix}^2, \quad \text{(A6)}$$

$$\Delta E_{so}^{nl}[(jK)_J] = \langle [(ls)j,l']K,s',J|h_{so}(nls)|[(ls)j,l']K,s',J\rangle = (-1)^{j+l+s+1} \begin{Bmatrix} j & l & s \\ 1 & s & l \end{Bmatrix} \times \varsigma_{nl}[(3/2)l(l+1)(2l+1)]^{1/2}, \quad \text{(A7)}$$

$$\Delta E_{so}^{n'l'}[(jK)_J] = \langle [(ls)j,l']K,s',J|h_{so}(n'l's')|[(ls)j,l']K,s',J\rangle = (-1)^{J+j+2K+l'+s'} \varsigma_{n'l'}[(3/2)l'(l'+1) \times (2l'+1)]^{1/2} \begin{Bmatrix} K & K & 1 \\ l' & l' & j \end{Bmatrix} \begin{Bmatrix} K & K & 1 \\ s' & s' & J \end{Bmatrix}. \quad \text{(A8)}$$

*knuroh@kent.edu

[1] L. Genzel, T. P. Martin, and U. Kreibig, Z. Phys. B **21**, 339 (1975).
[2] B. N. J. Persson and N. D. Lang, Phys. Rev. B **26**, 5409 (1982).
[3] B. N. J. Persson and E. Zaremba, Phys. Rev. B **31**, 1863 (1985).
[4] S. Tougaard, Surf. Interface Anal. **11**, 453 (1988).
[5] K. Nuroh, J. Phys. C **20**, 5305 (1987).
[6] J. M. Auerhammer and P. Rez, Phys. Rev. B **40**, 2024 (1989).
[7] H. R. Moser and G. Wendin, Phys. Rev. B **44**, 6044 (1991).
[8] K. Nuroh, Phys. Rev. B **77**, 125137 (2008).
[9] D. K. Saldin and Y. Ueda, Phys. Rev. B **46**, 5100 (1992).
[10] S. Polizzi, F. Antonangeli, G. Chiarello, and M. de Crescenzi, Surf. Sci. **136**, 555 (1984).
[11] S. G. Slusky, P. C. Gibbons, S. E. Schnatterly, and J. R. Fields, Phys. Rev. Lett. **36**, 326 (1976).
[12] J. R. Fields, P. C. Gibbons, and S. E. Schnatterly, Phys. Rev. Lett. **38**, 430 (1977).
[13] R. D. Leapman and L. A. Grunes, Phys. Rev. Lett. **45**, 397 (1980).
[14] R. D. Leapman, L. A. Grunes, and P. L. Fejes, Phys. Rev. B **26**, 614 (1982).
[15] J. Cazaux and A. G. Nassiopoulos, Surf. Sci. **162**, 965 (1985).
[16] J. A. D. Matthew, G. Strasser, and F. P. Netzer, Phys. Rev. B **27**, 5839 (1983).
[17] F. P. Netzer, G. Strasser, and J. A. D. Matthew, Phys. Rev. Lett. **51**, 211 (1983).
[18] G. Strasser, F. P. Netzer, and J. A. D. Matthew, Solid State Commun. **49**, 817 (1984).
[19] Y. Ohno, Phys. Rev. B **36**, 7500 (1987).
[20] K. Nuroh, Phys. Rev. B **70**, 205115 (2004).
[21] R. D. Cowan, *The Theory of Atomic Structure and Spectra* (University of California Press, Berkeley, 1981).
[22] L. Lozzi, M. Passacantando, P. Picozzi, S. Santucci, M. Diociaiuti, and M. de Crescenzi, Solid State Commun. **83**, 921 (1992).
[23] A. P. Hitchcock and C. H. Teng, Surf. Sci. **149**, 558 (1985).
[24] N. K. del Grande, Phys. Scr. **41**, 100 (1990).
[25] J. E. Müller, O. Jepsen, and J. W. Wilkins, Solid State Commun. **42**, 365 (1982).
[26] G. Wendin and K. Nuroh, Phys. Rev. Lett. **39**, 48 (1977).
[27] R. L. Park and J. E. Houston, Phys. Rev. B **6**, 1073 (1972).
[28] F. M. F. de Groot, J. Electron Spectrosc. Relat. Phenom. **67**, 529 (1994).
[29] B. T. Thole and G. van der Laan, Phys. Rev. B **38**, 3158 (1988).
[30] W. G. Waddington, P. Rez, I. P. Grant, and C. J. Humphreys, Phys. Rev. B **34**, 1467 (1986).
[31] S. Asada, C. Satako, and S. Sugano, J. Phys. Soc. Jpn. **37**, 855 (1975).
[32] R. P. Gupta and S. K. Sen, Phys. Rev. B **10**, 71 (1974).
[33] R. P. Gupta and S. K. Sen, Phys. Rev. B **12**, 15 (1975).
[34] T. Yamaguchi and S. Sugano, J. Phys. Soc. Jpn. **42**, 1949 (1977).
[35] I. P. Grant, B. J. McKenzie, P. M. Norrington, D. F. Mayers, and

N. C. Pyper, Comput. Phys. Commun. **21**, 207 (1980).
[36] K. G. Dyall and I. P. Grant, J. Phys. B **17**, 1281 (1984).
[37] T. Riedl, T. Gemming, and K. Wetzig, Ultramicroscopy **106**, 284 (2006).
[38] T. Riedl, T. Gemming, W. Gruner, J. Acker, and K. Wetzig, Micron **38**, 224 (2007).
[39] I. Lindgren and J. Morrison, *Atomic Many-Body Theory* (Springer-Verlag, Berlin, 1986).
[40] A. P. Jucys (Yutsis), I. B. Levinson, and V. V. Vanagas, *Mathematical Apparatus of the Theory of Angular Momentum* (Israel Program for Scientific Translation, Jerusalem, 1962), English translation.